

Design of New Wavelet Packets Adapted to High-Resolution SAR Images With an Application to Target Detection

Ammar Mian[✉], *Student Member, IEEE*, Jean-Philippe Ovarlez, *Member, IEEE*,
Abdourrahmane Mahamane Atto[✉], *Senior Member, IEEE*, and Guillaume Ginolhac[✉], *Member, IEEE*

Abstract—High resolution in synthetic aperture radar (SAR) leads to new physical characterizations of scatterers which are anisotropic and dispersive. These behaviors present an interesting source of diversity for target detection schemes. Unfortunately, such characteristics have been integrated and have been naturally lost in monovariate single-look SAR images. Modeling this behavior as nonstationarity, wavelet analysis has been successful in retrieving this information. However, the sharp-edge of the used wavelet functions introduces undesired high side-lobes for the strong scatterers present in the images. In this paper, a new family of parameterized wavelets, designed specifically to reduce those side lobes in the SAR image decomposition, is proposed. Target detection schemes are then explored using this spectro-angular diversity and it can be shown that in high-resolution SAR images, the non-Gaussian and robust framework leads to better results.

Index Terms—High resolution, robust adaptive detection, synthetic aperture radar (SAR), wavelet packets.

I. INTRODUCTION

A. Motivations

RADAR systems play a major role in modern military applications, air and ground traffic control, autonomous vehicles, observation of earth and other planetary systems, monitoring of dynamic objects such as forests, glaciers, meteors, and so on. An intelligent operational radar vision system involves self-tuned parameterization of the radar waveform emission (pulsewidth and repetition interval, transmitter power, etc.) and optimal target detection/characterization for automatic perception of a monitored environment. This requires self-coordination of the transmitter

and receiver which can operate in open or closed loops. This also requires integrating in radar-based machine intelligence frameworks, the capability of learning new/unknown radar waveforms. On the contrary, when considering earth observation from satellites using synthetic aperture radars (SARs), mainly artificial intelligence frameworks are developed in order to process the data obtained for various applications.

The SARs are moving radars systems capable of producing high-quality images of the earth's surface [1]. They consist in emitting an electromagnetic wave that is reflected on the earth's surface. The backscattered signal, which is affected by the scatterers on the surface, is then processed to build an image of the scene. SAR systems are known for their usability in all weather and illumination situations. They are, thus, capable to monitor all kind of areas of interest. Recent years have seen an increase in the number of SAR systems. Missions such as Sentinel-1 or TerraSAR-X have, for example, a global coverage of the earth's surface with SAR electronic imaging technology.

New missions in peculiar have a large bandwidth and an increased spatial resolution. In this context, specific responses of the scatterers have been observed. They are anisotropic and dispersive [2], [3] in contrast to the usual isotropic and whiteness assumption made in traditional SAR reconstruction algorithms. When considering high-resolution (HR) monovariate SAR images, a dispersion of the energy is observed. A single scatterer may have many side lobes on the reconstructed image. Moreover, the specific spectroangular response of the scatterer is naturally lost during the conventional SAR processing. This information is of interest and can be exploited as an additional source of diversity in many applications.

In SAR images processing, depending on the application, three important techniques are usually relied upon: target detection, segmentation, and classification. Target Detection schemes [4] consist in deciding if a target of interest is present at a given position of the image. Segmentation [5], [6], aim's is to delimit the image into segments which are conceptually meaningful such as the boundary between land and sea. Finally, classification [7]–[10] allows to label part of the images with regards to an application of interest. This paper focuses on target detection schemes and more specifically,

Manuscript received March 26, 2018; revised July 14, 2018 and November 19, 2018; accepted December 17, 2018. Date of publication January 14, 2019; date of current version May 28, 2019. This work was supported by the French National Agency of Research through PHOENIX under Grant ANR-15-CE23-0012. (Corresponding author: Ammar Mian.)

A. Mian is with Sonda, CentraleSupélec, Université Paris-Saclay, 91190 Gif-sur-Yvette, France, and also with LISTIC Lab, Université Savoie Mont Blanc, 74940 Annecy, France (e-mail: ammar.mian@centralesupelec.fr).

J.-P. Ovarlez is with Sonda, CentraleSupélec, Université Paris-Saclay, F-91190 Gif-sur-Yvette, France, and also with DEMR, ONERA, Université Paris-Saclay, F-91123 Palaiseau, France.

A. M. Atto and G. Ginolhac are with LISTIC Lab, Université Savoie Mont Blanc, 74940 Annecy, France.

Color versions of one or more of the figures in this paper are available online at <http://ieeexplore.ieee.org>.

Digital Object Identifier 10.1109/TGRS.2018.2888993

on schemes which respect the constant false alarm (CFAR) property [11]. This property allows detecting targets while guaranteeing a certain probability of false alarm.

B. Relation to Prior Works

Classic schemes usually rely on a diversity of some sort to characterize the target and to separate it from the clutter. The literature on the subject concerning SAR images is vast as many kinds of diversities can be exploited. For example, in [4], a spatial template model of the target is used in likelihood ratio schemes to derive detectors. Polarimetric diversity has been used in [12] and [13] to detect vehicles under foliage, in [14] to detect ship in sea clutter, or in [15] and [16] for segmentation purposes. In [17] a diversity coming from successive pulses is used to detect range-spread targets. In [18]–[20], time-division multiplexing of the antennas is exploited to create diversity for ground moving targets identification. An extension to non-Gaussian model has been explored in [21]–[23].

In this paper, the spectroangular behavior mentioned earlier as a source of diversity is considered. Several works have investigated the methods for retrieving the spectroangular diversity. For example, approach such as steerable pyramids [24], [25], curvelets [26], or subspaces [27], [28] are possible. However, they are usually heavy methods. For example, subspace methods have high-computational cost and are not adaptive. They also assume the knowledge of a physical model, which makes them specific to an application. Time–frequency analysis is a simpler approach that allows analyzing the SAR data to retrieve nonstationary information such as spectral and angular behaviors. This approach was used in [39] and [40], where the azimuth bandwidth has been separated in two subbands for ship detection. In the following, we restrict only on the linear time–frequency distributions (LTFDs) as they allow to keep the phase information and the possibility to apply the reconstruction property.

Wavelet decomposition of SAR images has been studied for many applications. In [30] and [31], wavelet frames have been used in order to derive a measure of the polarimetric texture used in segmentation and target detection schemes. Wavelet transforms on SAR images have been used in [32] to retrieve wind fields. In [33], wavelets have been used to reduce speckle noise in interferometric SAR images. Fusion techniques on wavelet coefficients have been used in [34] in order to compute a change detection map. Wavelet decomposition associated with kurtosis statistics have been exploited in [6] and [7] for both segmentation and classification purposes. In [35] and [36], multiresolution information is used for target detection schemes in Gaussian context. Retrieval of spectroangular diversity using wavelet decomposition have in peculiar been investigated in work such as [37], [38]. More precisely, these methods have been used for target detection applications in [39] or for change detection in [40]. In those works, the spectroangular information has presented promising results. However, in those works, the decomposition induced side lobes on the subimages which may decrease the performance.

This paper proposes a wavelet packet formalism (as a generalization of LTFD) and designs a new family of wavelets aimed at decreasing these side lobes. Then, the multivariate image resulting from the wavelet decomposition is modeled by a multivariate statistical framework. This framework allows retrieving the properties of the clutter through a covariance matrix parameter. Using this modeling, classic adaptive methods can be used in order to detect a target embedded in clutter disturbances. The spectroangular behavior of the target is assumed to be known through a steering vector. These adaptive methods have been extensively studied in [41] and [42], where the disturbances are modeled as a realization of a Gaussian random variable parameterized by an unknown covariance matrix. Classically, secondary data, assumed to be free of the target, corresponding to surrounding pixels are used for the estimation of the covariance matrix. Since in this paper the images are the result of wavelet decomposition, the size of the vector is expected to be large. Clearly, when the size of the vectors is large, the number of secondary data needed increases. This is problematic in HR SAR images where heterogeneity of the data is naturally present. In this case, the hypothesis of homogeneity of the surrounding pixels is not evident and the Gaussian model reflects poorly the observations. Robust methods have been developed using broader families of distributions than the Gaussian one [43], [44]. In this paper, both Gaussian and robust methods will be studied and compared.

C. Contributions of this Paper

The different contributions of this paper are summarized as follows.

- 1) A parametrized wavelet family is proposed to analyze SAR Images. The new family is an extension of Shannon M-Band filters that are adapted to take into account SAR geometry. The new family is designed to reduce side lobes on the wavelet coefficients. A criterion is proposed for the choice of its parameters.
- 2) The spectroangular diversity, obtained through wavelet decomposition, is used in robust target detection schemes. Target detection schemes are explored in both Gaussian and elliptical noise assumption and are studied through two alternatives CFAR detectors: the adaptive matched filter (AMF) and the adaptive normalized matched filter (ANMF). The behavior of those detectors in terms of regulation of false alarm and performance of detection are compared using two separate data sets.

D. Paper Organization

This paper is organized as follows. In Section II, the acquisition geometry of SAR is recalled and it is explained how the information about anisotropy and dispersivity of scatterers is lost in the processing of the single-look monovariate image. Then, in Section III, Shannon M-band wavelets are adapted for the purpose of retrieving spectroangular diversity in SAR images. In Section IV, an application of wavelet decomposition to target detection is presented and in Section V, simulations and results are presented. Finally, some conclusions are drawn in Section VI. Proofs are given in Appendices.

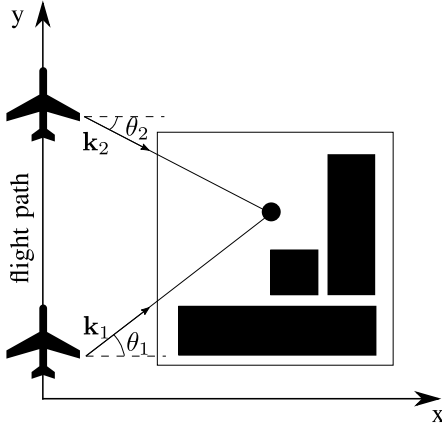


Fig. 1. SAR acquisition geometry. A reflector is viewed at two different angles of illumination θ_1 and θ_2 in a given frequency. This information is summarized through the wave vectors \mathbf{k}_1 and \mathbf{k}_2 .

The following conventions are adopted: matrices are in bold and capital, vectors in bold. \mathbb{R}^N and \mathbb{C}^N refer to the sets of N -dimensional real and complex vectors. $L^n(\mathbb{C}^2)$ is the set of the functions having values in \mathbb{C}^2 for which the n th power of the absolute value is integrable. For a given complex scalar, $\bar{\cdot}$ denotes the conjugate operator, $|\cdot|$ is the module operator. For any given vector or matrix, \cdot^T denotes the transpose operator, \cdot^H denotes the transpose conjugate operator, $\|\cdot\|$ is the Euclidean norm. For any matrix, $|\cdot|$ denotes the determinant. Given a 2-D function $g \in L^1(\mathbb{C}^2) \cup L^2(\mathbb{C}^2)$, the 2-D Fourier transform (respectively inverse Fourier Transform) is denoted by $\mathcal{F}g(\omega_1, \omega_2) = \int_{\mathbb{R}} g(x_1, x_2) e^{-i\omega_1 x_1} e^{-i\omega_2 x_2} dx_1 dx_2$ (respectively $\mathcal{F}^{-1}g$) and define $\tau_{[p,q]}g(x, y) = g(x-p, y-q)$. For a function, $\langle \cdot, \cdot \rangle$ is the inner product on $L^1(\mathbb{C}^2) \cup L^2(\mathbb{C}^2)$ and $\|\cdot\|$ is the L^2 norm. \mathbb{I}_K denotes the indicator function of a given set K .

II. SAR IMAGE AND NONSTATIONARITIES

In this section, we describe the geometry of acquisition for a SAR system and give the definition of relevant physical parameters. We then explain how algorithms such as range migration algorithm (RMA) result in a loss of information when considering HR SAR image.

A. SAR Acquisition Geometry

Fig. 1 presents the geometry of acquisition for an SAR system. The moving radar transmits an electromagnetic wave represented by the wave vector $\mathbf{k} = [k_x, k_y]^T$ and recovers the backscattering signal in order to obtain a map of the reflectors of the scene. \mathbf{k} is related to the emitted frequency f by $\|\mathbf{k}\| = \mathfrak{K} = 2f/c$, c being the celerity of the light, and to the angle of illumination θ by $\theta = \arctan(k_y/k_x)$.

The emitted signal is located in a certain range of frequencies defined by: $[f_0 - B/2, f_0 + B/2]$, f_0 being the carrier and B being the bandwidth of the radar. This translates in terms of spatial frequencies \mathfrak{K} to: $[\mathfrak{K}_0 - \mathfrak{K}_B/2, \mathfrak{K}_0 + \mathfrak{K}_B/2]$ with $\mathfrak{K}_0 = 2f_0/c$, $\mathfrak{K}_B = 2B/c$. The angles θ of illumination lies in $[-\theta_B, \theta_B]$ angular domain. The spatial SAR resolutions

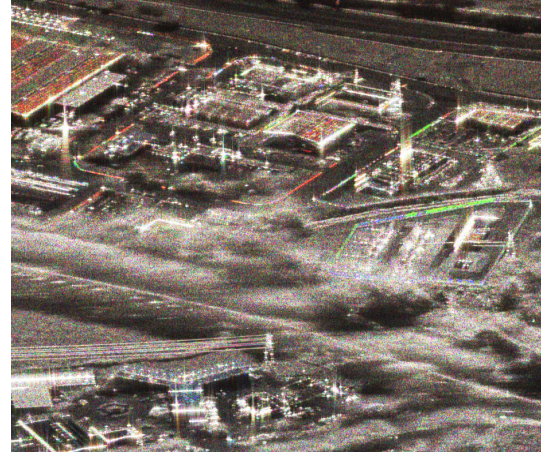


Fig. 2. ONERA RGB color-coded SAR image acquired for three consecutive frequency bands.

are given, respectively, in azimuth by $\delta_y = c/(4f_0\theta_B)$ and in radial range by $\delta_x = c/(2B)$. We define $\mathcal{D} = [\mathfrak{K}_0 - \mathfrak{K}_B/2, \mathfrak{K}_0 + \mathfrak{K}_B/2] \times [-\theta_B, \theta_B]$, and $\mathbf{U}^{\mathcal{S}, \mathcal{A}}$ as the space of functions having spectroangular features in \mathcal{D} .

B. Anisotropy and Dispersivity of Scatterers

In HR SAR Images, the hypothesis of isotropy and nondispersivity of the scatterers is no longer obvious. When a target is illuminated using a large bandwidth and a large range of angles, it is more reasonable to assume that its response is dependent on the wave vector. Recent studies of the spectral and angular behavior of the scatterers have shown the variation of the scatterers' response for several angles of illumination and several frequencies [2], [45].

Fig. 2 presents an ONERA SAR image in X-band. The responses of the scene relative to three consecutive frequency bands have been coded in RGB color-coding. Red points are responding only on the first band, green ones on the second band, and the blue ones on the third band. They are called colored scatterers. Gray points are called white scatterers as they are responding equivalently in the three subbands. This image perfectly illustrates how some scatterers have different behavior given the band used. Similar results can be achieved when looking at the scene at a different range of angles. This diversity is of interest as it can be interpreted in terms of target characteristic: given the spectroangular behavior of an object of interest, one can adapt target detection schemes on multivariate SAR images to this specific behavior.

Unfortunately, for complex monovariate SAR images, this information is lost during the processing. In algorithms such as RMA [1], the aim is to collect a backscattering reflection coefficient $\tilde{I}(\mathbf{k})$ and then perform Fourier-based spectral estimation in order to build the conventional complex single-look (monovariate) SAR image $I(\mathbf{r})$ for each point $\mathbf{r} = [x, y]^T$ on the ground

$$I(\mathbf{r}) = \int_{\mathcal{D}} \tilde{I}(\mathbf{k}) \exp(2i \pi \mathbf{k}^T \mathbf{r}) d\mathbf{k} \quad (1)$$

where the integration is performed on the whole spectral and angular domains. When colored scatterers are present, their spectroangular behavior is effectively lost.

Works such as [37] or [38] have proposed to model the nonstationarities of the scatterers of the image I in the space of spectral and angular features $[\mathfrak{R}, \theta]$. Using this model, wavelet analysis is a powerful tool for analyzing the behavior of the colored scatterers. For instance, an hyperimage representing the reflectivity of the scene for any subspace $\mathcal{E} \subset \mathcal{D}$ is given as

$$\tilde{I}_{\mathcal{E}}(\mathbf{r}) = \int_{\mathcal{E}} \tilde{I}(\mathbf{k}) \overline{\Psi_{\mathcal{E}}^S(\mathbf{k}, \mathbf{r})} d\mathbf{k} \quad (2)$$

where $\Psi_{\mathcal{E}}^S(\mathbf{k}, \mathbf{r})$ is a wavelet function with spectro-angular support \mathcal{E} . When considering several subsets $\mathcal{E}_1, \dots, \mathcal{E}_M$, a wavelet packet $\{\Psi_{\mathcal{E}_i}^S(\mathbf{k}, \mathbf{r})/i = 1, \dots, M\}$ can be defined. The problematic is then to choose the shape of the wavelets and a relevant partition of \mathcal{D} in terms of \mathcal{E}_i as to decompose the image in separate frequency bands and range of angles for a given purpose.

This approach was used in [39], [40] where good results in both target detection and change detection have been obtained. However, in those works, the problem of side lobes has not been considered. We propose in Section III to design new wavelets aimed at reducing the dispersion of energy on the subimages.

III. NEW WAVELET DESIGN FOR SAR ANALYSIS

In this section, new wavelet packets adapted to SAR geometry are developed. The particularity of this new packet with regards to existing literature is the choice of polar representation which better describes the data with regards to the spectroangular diversity of interest. To this end, we use classic Shannon M-band filters that we adapt to take into account the spectral support of SAR Images and then we correct the edge effects of those wavelets.

The adaptation of wavelet packets in this geometry can be done using many classic wavelets packets (Gabor, Debaucheries, etc.). However, Shannon M-band filters have been chosen as a basis of our design for the following reasons.

- 1) They are separable with regards to the two dimensions (\mathfrak{R}, θ) of the decomposition, which makes them ideal when we want to choose the number of subbands and sublooks (as in looking angle) separately.
- 2) Since we expect to exploit the decomposition in classic target detection scheme, there is a need for each coefficient to deliver different information than the others. Otherwise, correlations between subbands/sublooks would be introduced due to the shape of the wavelets and may deteriorate detection performance. This leads to a choice of an orthogonal wavelet packet.
- 3) To better describe the behavior of a possible target as a function of the frequencies and looking angle, we consider wavelets corresponding to a connected subset of the frequency/angular domain.

A. Shannon M-Band Wavelets Theory

Let M_1 and M_2 be natural numbers that are both greater than or equal to 2. The Shannon 2-D $M_1 \times M_2$ multiband wavelet filters used in this paper follow from a separable 2-D extension of 1-D filters presented in [46] and [47]. These filters give a multiresolution framework for decomposing any image.

We define \mathbf{U}^S as the 2-D Paley–Wiener (PW) space composed by elements of $L^2(\mathbb{R}^2)$ whose Fourier transform is supported within $[-\pi, \pi]^2$. Any element of this space satisfies Shannon's sampling theorem. Therefore, when the $M_1 \times M_2$ multiband decomposition concerns the PW space \mathbf{U}^S , the input data for the decomposition of any element g of this functional space are the samples $\{g[k, \ell]\}_{k, \ell \in \mathbb{Z}}$ of g (corresponding to the pixels of the image to decompose).

The 2-D Shannon wavelet packet function at resolution level j and 2-D shift parameters (n_1, n_2) , with $n_{\varepsilon} \in \{0, \dots, M_{\varepsilon}^j - 1\}$ for $\varepsilon \in \{1, 2\}$, is given as

$$\Psi_{j, [n_1, n_2]}^S = M_1^{j/2} M_2^{j/2} \mathbb{I}_{\Delta_{j, G^{[1]}(n_1)}^0 \times \Delta_{j, G^{[2]}(n_2)}^1} \quad (3)$$

where

$$\Delta_{j, k}^{\varepsilon} = \left[-\frac{(k+1)\pi}{M_{\varepsilon}^j}, -\frac{k\pi}{M_{\varepsilon}^j} \right] \cup \left[\frac{k\pi}{M_{\varepsilon}^j}, \frac{(k+1)\pi}{M_{\varepsilon}^j} \right] \quad (4)$$

and $(G^{[\varepsilon]})_{\varepsilon \in \{1, 2\}}$ are the permutation maps defined, respectively, for $\varepsilon \in \{1, 2\}$, by $G^{[\varepsilon]}(0) = 0$ and by recursively setting, for $k = 0, 1, \dots, M_{\varepsilon} - 1$ and $\ell = 0, 1, 2, \dots$

$$G^{[\varepsilon]}(M\ell + k) = \begin{cases} MG^{[\varepsilon]}(\ell) + k, & \text{if } G^{[\varepsilon]}(\ell) \text{ is even} \\ MG^{[\varepsilon]}(\ell) - k + M - 1, & \text{if } G^{[\varepsilon]}(\ell) \text{ is odd.} \end{cases} \quad (5)$$

Define $\Phi_{j, [n_1, n_2]}^S = \mathcal{F}^{-1} \Psi_{j, [n_1, n_2]}^S$. A 2-D wavelet packet subspace $\Phi_{j, [n_1, n_2]}^S$ is generated as the closure of the space spanned by the following translated versions of $\Phi_{j, [n_1, n_2]}^S$:

$$\Phi_{j, [m, n]}^S = \text{Clos} \left\{ \tau_{[M_1^j p, M_2^j q]} \Phi_{j, [m, n]}^S : p \in \mathbb{Z}, q \in \mathbb{Z} \right\}. \quad (6)$$

These subspaces are such that for any fixed j

$$\mathbf{U}^S = \bigoplus_{\substack{m=0, 1, \dots, M_1^j - 1 \\ n=0, 1, \dots, M_2^j - 1}} \Phi_{j, [m, n]}^S$$

where \oplus denotes the direct sum of functional subspaces.

As an illustration, the Shannon 2×3 multiband wavelet packet tree is given by Fig. 3 as a tree product resulting from a 2-band and a 3-band 1-D trees, where the tree product involves all combination of nodes given at a fixed resolution level j . In this figure, the positive part $\Delta_{j, k}^{\varepsilon, +}$ of $\Delta_{j, k}^{\varepsilon}$ is given for each resolution level j under consideration.

The Shannon $M_1 \times M_2$ multiband coefficients of the projection of g on a 2-D wavelet packet subspace $\Phi_{j, [n_1, n_2]}^S$ defines the wavelet coefficients

$$\mathbf{C}_{j, [n_1, n_2]}^S[p, q] = \iint_{\mathbb{R}^2} g(z, t) \tau_{[M_1^j p, M_2^j q]} \Phi_{j, [n_1, n_2]}^S(z, t) dz dt. \quad (7)$$

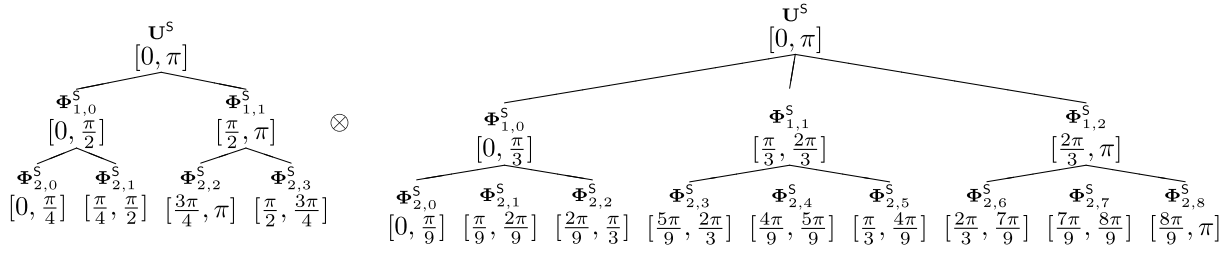


Fig. 3. Shannon 2×3 multiband decomposition tree associated with $j = 2$. The positive part of $\Delta_{j,\bullet}^{1,+}$ of $\Delta_{j,\bullet}^1$ are given in the left-side tree whereas $\Delta_{j,\bullet}^{2,+}$, positive part of $\Delta_{j,\bullet}^2$, are given at the right-side tree. The frequency tiles associated with the decomposition are the intervals $\Delta_{j,\bullet}^1 \times \Delta_{j,\bullet}^2$ for every fixed j : the whole tree involves all combination of nodes given at a fixed resolution level j .

Proposition 1: The coefficients of the projection of g on a wavelet packet subspace $\Phi_{j,[n_1,n_2]}^S$ is a discrete sequence $\mathbf{C}_{j,[n_1,n_2]} = (\mathbf{C}_{j,[n_1,n_2]}^S[p, q])_{p,q \in \mathbb{Z}}$, where

$$\mathbf{C}_{j,[m,n]}^S[p, q] = M_1^{-j/2} M_2^{-j/2} \mathcal{F}^{-1} U_{j,[m,n]}(M^j p, M^j q) \quad (8)$$

with

$$U_{j,[m,n]} = [\mathcal{F}g] \times \mathbb{I}_{\Delta_{j,G(m)}^0 \times \Delta_{j,G(n)}^1}. \quad (9)$$

Proof: See Appendix A. \square

In practice, g is a discrete image to be decomposed. This proposition shows how wavelet coefficients can be easily obtained in practice through a simple fast Fourier transform (FFT). $[p, q]$ are the pixels of the wavelet coefficient for shift parameters $[n_1, n_2]$ at a fixed resolution j . Note that a decomposition at a given resolution j assume that the wavelets coefficients correspond to a decimated version of the image (by a factor of M_1^j and M_2^j). This methodology allows computing efficiently the coefficients with a low-complexity. Indeed, since only a Hadamard product and an FFT are necessary, the complexity is linear with regards to the number of coefficients desired.

The wavelets presented here are designed for images respecting Shannon sampling theorem. The decomposition is done on functions whose frequencies are contained in the space $[-\pi, \pi]^2$. We adapt hereafter Shannon wavelets from the Cartesian space $[-\pi, \pi]^2$ to the polar space \mathcal{D} corresponding to the physical diversity of interest for SAR images.

B. Adaptation of Shannon Wavelets to SAR Geometry

Define

$$\Psi_{j,[m,n]}^{S,\angle}(\mathbf{R}, \theta) = R^{j/2} L^{j/2} \mathbb{I}_{\Delta_{j,\mathbf{R}_m} \times \Delta_{j,\theta_n}}(\mathbf{R}, \theta) \quad (10)$$

where

$$\Delta_{j,\mathbf{R}_m} = \mathbf{R}_0 - \mathbf{R}_B + \left[\frac{m\mathbf{R}_B}{R^j}, \frac{(m+1)\mathbf{R}_B}{R^j} \right] \quad (11)$$

$$\Delta_{j,\theta_n} = \left[\frac{n\theta_B}{L^j}, \frac{(n+1)\theta_B}{L^j} \right]. \quad (12)$$

From this, we define the wavelet functions $\Phi_{j,[m,n]}^{S,\angle}(x, y) = \mathcal{F}^{-1} \Psi_{j,[m,n]}^{S,\angle}(\mathbf{R}, \theta)$. Here, the variables x and y correspond to the range and cross-range position as in Fig. 1. Note that this definition requires computing the Fourier transform on spectral and angular variables. Among the different possible

solutions of this problem, we will use interpolation from the fractional FFT (3FT) in order to fill the Polar grid $[\mathbf{R}_0 - \mathbf{R}_B/2, \mathbf{R}_0 + \mathbf{R}_B/2] \times [-\theta_B, \theta_B]$ from the Cartesian one corresponding to variables k_x and k_y . Among the 3FT implementations, we recommend using that of [48].

The wavelets thus defined constitute a wavelet packet as per the following proposition.

Proposition 2 (Vanishing Moments): For any nonnegative integers j, m, n, p, q , we have

$$\iint_{\mathbb{R}^2} x^p y^q \Phi_{j,[m,n]}^{S,\angle}(x, y) dx dy = 0.$$

Proof: See Appendix B. \square

Functions $\Phi_{j,[m,n]}^{S,\angle}$ defined above have, thus, an infinite number of vanishing moments. Since they are well localized in space/frequency/angle, they are wavelet functions.

Define the wavelet subspaces $\Phi_{j,[m,n]}^{S,\angle}$ similar to (6). Then, we have the following.

Proposition 3 (Orthogonality of Wavelet Packet Subspaces): For any given j and any $(m, n) \neq (m', n')$, we have

$$\Phi_{j,[m,n]}^{S,\angle} \perp \Phi_{j,[m',n']}^{S,\angle}$$

where \perp denotes orthogonality symbol.

Proof: See Appendix B. \square

Proposition 4 (Completion of Wavelet Packet Subspaces): For any given j , and any (m, n) , we have

$$\bigcup_{\substack{m=0, 1, \dots, R^j-1 \\ n=0, 1, \dots, L^j-1}} \Phi_{j,[m,n]}^{S,\angle} = \mathbf{U}^{S,\angle}.$$

Proof: See Appendix B. \square

Propositions 2, 3 and 4 highlight that wavelet subspaces $\Phi_{j,[m,n]}^{S,\angle} : j \geq 1, m = 0, 1, \dots, R^j - 1, n = 0, 1, \dots, L^j - 1$ can thus be used to define several multiresolution frameworks (specific subselection of j, m, n) for analyzing SAR data.

Analyzing SAR data is done by computing the wavelet coefficients as previously stated in (2). We have the following.

Proposition 5 (Wavelet Coefficients): In practice, at a resolution level j , we obtain the wavelet coefficients by computing the following:

$$\mathbf{C}_{j,[m,n]}^{S,\angle}[p, q] = R^{-j/2} L^{-j/2} \mathcal{F}^{-1} V_{j,[m,n]}(R^j p, L^j q) \quad (13)$$

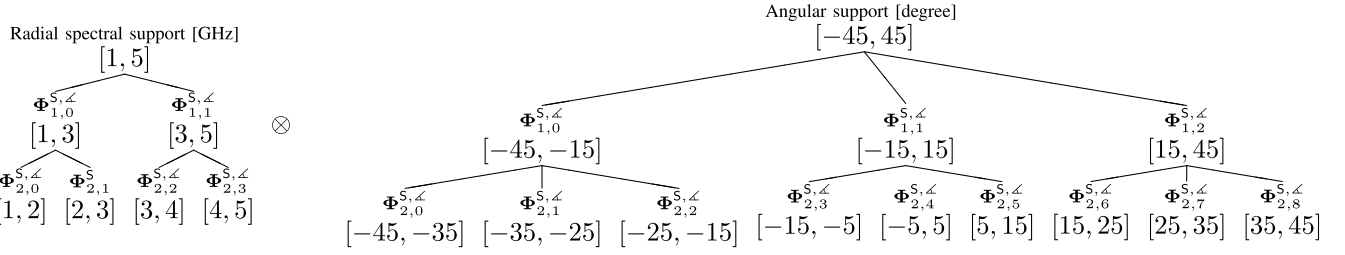


Fig. 4. Cartesian product \otimes of spectral and angular multiresolution trees associated with radial “2 bands–2 resolutions” and angular “3 looks–2 resolutions” splitting $\Psi_{j,[m,n]}^{S,\angle}(\mathcal{R}, \theta)$ defined by (16) when considering $[f_0 - B/2, f_0 + B/2] \times [-\theta_B, \theta_B] = [1 \text{ GHz}, 5 \text{ GHz}] \times [-45 \text{ deg}, 45 \text{ deg}]$. The intervals represented are given for illustration.

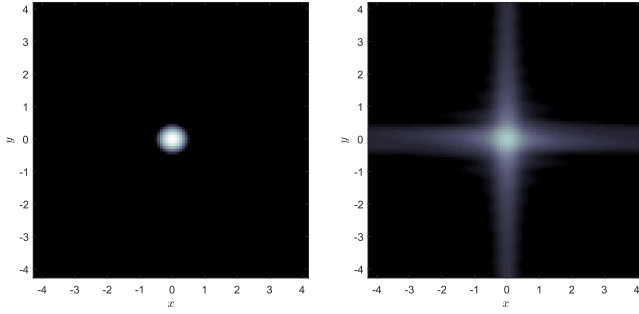


Fig. 5. Example of bright point decomposition. (Left) Image I . (Right) $C_{1,[1,1]}^{S,\angle}$ with $R = L = 2$.

where $V_{j,[m,n]}$ follows from the backprojection of the SAR image with respect to spectral and illumination features

$$V_{j,[m,n]}(\mathcal{R}, \theta) = \tilde{I}(\mathcal{R}, \theta) \mathbb{I}_{\Delta_{j,\mathcal{R}_m} \times \Delta_{j,\theta_n}}(\mathcal{R}, \theta). \quad (14)$$

Proof: Similar to proposition 1. \square

Again, the complexity of this methodology is linear with regards to the number of coefficients ($R \times L$) since coefficients are obtained from a Hadamard product and a 3FT. In practice, any SAR data can efficiently be analyzed using this methodology.

An example of a multiresolution analysis is given in Fig. 4 for spectral features and angular illumination in $[f_0 - B/2, f_0 + B/2] \times [-\theta_B, \theta_B] = [1, 5] \text{ GHz} \times [-45, 45] \text{ deg}$.

C. Bell-Shaped Wavelets Design for SAR Geometry

When considering Shannon wavelets, the decomposition is subject to hard transition in the sense that each filter is an ideal bandpass filter. When considering the wavelet coefficients, this results in convolution with a sinc function which has high side lobes (see Fig. 5 for an illustration). This dispersion of energy is problematic in detection schemes when secondary data, corresponding to the surrounding pixels, are needed.

To limit the side lobes on the wavelet coefficients which are due to the sharp edge of the Shannon wavelets, we look for alternatives that are subject to smooth transitions. We derive hereafter, a new family of parameterized R-band/L-look wavelet functions including the Shannon wavelets as limit case.

We propose the following criteria for the design of the new family of wavelets.

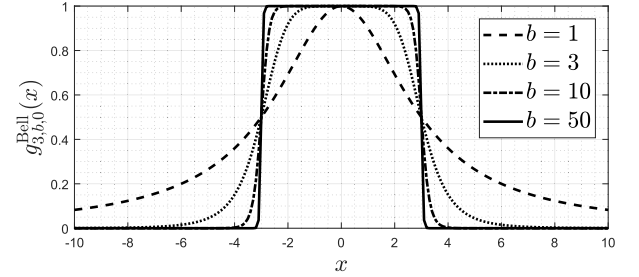


Fig. 6. Bell-shaped function with width $a = 3$, center $c = 0$, and different slope parameters $b \in \{1, 3, 10, 50\}$.

- 1) Well located in frequencies and angles (wavelet function).
- 2) Similar behavior to Shannon wavelets to preserve the framework presented in III-B.
- 3) Smooth transition with a parameter controlling the decay (for adaptability purposes).

Many functions respect the two first criteria. However, Bell-shaped membership functions appear to be a good choice as they allow to control both center, extent, and slope (and thus smoothness). They are a family of 1-D functions defined by

$$g_{a,b,c}^{\text{Bell}}(x) = \frac{1}{1 + \left| \frac{x-c}{a} \right|^{2b}} \quad (15)$$

where the parameter a stands for the width of the function, the parameter b controls the slope, and the parameter c is a location parameter.

Fig. 6 gives an example of Bell function with different slopes and shows that these functions are good candidates for our problem. Using them as a basis, we define

$$\Psi_{j,[m,n]}^{[d_1,d_2],\angle}(\mathcal{R}, \theta) = R^{\frac{1}{2}} L^{\frac{1}{2}} H_{j,[m,n]}^{[d_1,d_2],\angle}(\mathcal{R}, \theta) \mathbb{I}_{\mathcal{D}} \quad (16)$$

where $H_{j,[m,n]}^{[d_1,d_2],\angle}$ is defined as a product of two Bell functions

$$H_{j,[m,n]}^{[d_1,d_2],\angle}(\mathcal{R}, \theta) = H_{j,m}^{d_1,\angle}(\mathcal{R}) H_{j,n}^{d_2,\angle}(\theta) \quad (17)$$

with

$$H_{j,m}^{d_1,\angle}(\mathcal{R}) = g_{\frac{\mathcal{R}_B}{2R^j}, d_1, \mathcal{R}_0 - \frac{\mathcal{R}_B}{2} + \frac{(2m+1)\mathcal{R}_B}{2R^j}}^{\text{Bell}}(\mathcal{R})$$

$$H_{j,n}^{d_2,\angle}(\theta) = g_{\frac{\theta_B}{L^j}, d_2, -\theta_B + \frac{(2n+1)\theta_B}{2L^j}}^{\text{Bell}}(\theta).$$

The definition is similar to that of (10): the center and width of Bell functions have been adapted to span the SAR geometry domain \mathcal{D} through R^j translations along $\hat{\mathbf{R}}$ and L^j translations along θ . The slope parameters d_1 and d_2 are let open as a parametrization of the wavelet family.

Define $\Phi_{j,[m,n]}^{[d_1,d_2],\angle} = \mathcal{F}^{-1} \Psi_{j,[m,n]}^{[d_1,d_2],\angle}(\hat{\mathbf{R}}, \theta)$, the wavelet function. We have the following properties.

Proposition 6 (Vanishing Moments): For any nonnegative integers j, m, n, p, q , we have

$$\iint_{\mathbb{R}^2} x^p y^q \Phi_{j,[m,n]}^{[d_1,d_2],\angle}(x, y) dx dy = 0.$$

Proof: Similar to 2. The null derivative in $(0, 0)$ is assured by the indicator $\mathbb{I}_{\mathcal{D}}$. \square

Proposition 6 indicates that the functions presented by (16) define wavelets.

Proposition 7 (Convergence to Shannon Wavelets): The R -band L -look wavelet transform obtained by using (16) is associated with the Shannon wavelet transform when $d_1, d_2 \rightarrow +\infty$

$$\lim_{d_1 \rightarrow +\infty} \lim_{d_2 \rightarrow +\infty} \Psi_{j,[m,n]}^{[d_1,d_2],\angle} \stackrel{\text{a.e.}}{=} \Psi_{j,[m,n]}^{\text{S},\angle} \quad (18)$$

where equality holds true almost everywhere (a.e.).

Proof: See Appendix C. \square

Proposition 7 highlights that the Bell-shaped wavelets have similar behavior than Shannon wavelets for high value of d_1 and d_2 and can thus be used for analyzing SAR images. For convenience purposes, we use alternatively the notation $\Psi_{j,[m,n]}^{[\infty,\infty],\angle} = \Psi_{j,[m,n]}^{\text{S},\angle}$.

A problem arises in the choice of these slope parameters. One can intuit that given their value, the properties of orthogonality and completion of wavelet packet subspaces are not assured. Unfortunately, given the expression of the wavelets, finding an interval of values using orthogonality or completion properties is not possible to our knowledge. As such, we propose to consider the wavelet packet in terms of frames (see [49] for details) which relax the conditions of orthogonality and completion. As suggested in [50], a wavelet packet has good reconstruction property if the energy of the signal is preserved when doing the decomposition and reconstruction. In practice, this can be ensured if the following condition is respected [51]:

$$Q(\hat{\mathbf{R}}, \theta) = \sum_{m,n} |H_{j,[m,n]}^{[d_1,d_2],\angle}(\hat{\mathbf{R}}, \theta)|^2 \approx 1 \quad \forall \hat{\mathbf{R}} \quad \forall \theta. \quad (19)$$

This criterion can be used to grasp qualitatively how the decomposition will treat the frequencies present in the image. If $Q > 1$, the energy increase which means that the packet is redundant. When $Q < 1$, there is a loss of energy and thus information. We propose to use this criterion to select the values of d_1 and d_2 which preserve energy the most.

Since the expression in (17) is separable in $\hat{\mathbf{R}}$ and θ , we can treat both separately and solve the problems: $\forall (\hat{\mathbf{R}}, \theta) \in \mathcal{D}$, find d_1 subject to $Q_{\hat{\mathbf{R}}}(\hat{\mathbf{R}}) = \sum_{m,n} |H_{j,[m,n]}^{d_1,\angle}(\hat{\mathbf{R}})|^2 \approx 1$ and find d_2 subject to $Q_{\theta}(\theta) = \sum_{m,n} |H_{j,[m,n]}^{d_2,\angle}(\theta)|^2 \approx 1$.

Fig. 7 gives the values of Q for several values of d_1 and d_2 for a given set of $(j, R, L, f_0, B, \theta_B)$. We note that for small

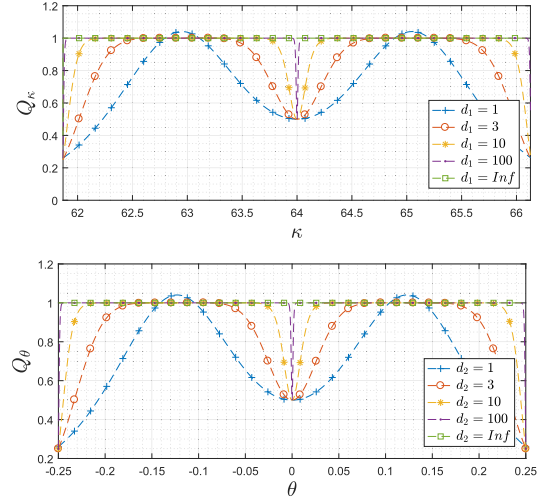


Fig. 7. Redundancy of wavelet packet for $f_0 = 9.6$ GHz, $B = 640$ MHz, $\theta_B = 0.25$ rad, $j = 1$, and $R = L = 2$.

values of $d_{\epsilon \in \{1,2\}}$, there is a loss of energy at the transitions between the filters. For values of $d_{\epsilon \in \{1,2\}} \in [10, \infty[$, this loss is acceptable. Indeed, since the wavelet packet is developed for target detection schemes, there is a need to know the spectroangular behavior in a vector of a fixed size. This means that if the energy of most of each band is preserved in the coefficients, this will not impact much the detection scheme.

Finally, we can compute the wavelets coefficients simply by taking expression at (13) and using $V_{j,[m,n]}(\hat{\mathbf{R}}, \theta) = \tilde{I}(\hat{\mathbf{R}}, \theta) H_{j,[m,n]}^{[d_1,d_2],\angle}$.

IV. APPLICATION TO TARGET DETECTION

In this section, we propose to use the wavelet decomposition of Section III in order to detect a target in a noisy SAR image. First, we give a statistical model for noise disturbances. Then, we present the target detection problem.

A. Data Model

In the following, each pixel location (p, q) of the SAR image will be represented, at a resolution level j , by a set of R -radius and L -look wavelets features encapsulated in the random complex vector

$$\mathbf{c}_j[p, q] \triangleq \{C_{j,[m,n]}^{[d_1,d_2],\angle}[p, q]\}_{m=0,1,\dots,R^j-1, n=0,1,\dots,L^j-1} \in \mathbb{C}^N$$

where $N = R^j \times L^j$.

In standard applications, the vector $\mathbf{c}_j[p, q]$ is modeled as a multivariate Gaussian vector: $\mathbf{c}_j[p, q]$ follows a Gaussian distribution $\mathcal{CN}(\mathbf{0}, \mathbf{R})$ where \mathbf{R} is the unknown covariance matrix of the data. This model is accurate for SAR images where each pixel is the sum of the contributions of all the scatterers inside its range.

However, when considering HR SAR images, the number of scatterers present in any pixel of the image is small, meaning that the Central Limit Theorem may no longer be applicable. Moreover, there are many nonstationarities inherent to this kind of images where the backscattered power can vary greatly spatially inside the analysis windows. Thus, the Gaussian

hypothesis may no longer be applicable. To generalize the Gaussian statistic, we assume that $\mathbf{c}_j[p, q]$ follows a complex elliptical symmetric (CES) distribution $\mathcal{CE}(\mathbf{0}, g, \mathbf{R})$ where the scatter matrix \mathbf{R} is unknown and where g stands for any characteristic function generator [52]. This model extends the Gaussian distribution and better characterizes HR SAR images.

In both models, the matrix \mathbf{R} characterizes the angular and the spectral behavior of each scatterer. To estimate this matrix, the following K secondary vectors surrounding the pixel (p, q) under test (supposed homogeneous in terms of angular and spectral behavior) are used:

$$\{\mathbf{c}_j[p - \ell_1, q - \ell_2]\}_{\substack{\ell_1=-K_1, \dots, K_1 \\ \ell_2=-K_2, \dots, K_2 \\ (\ell_1, \ell_2) \neq (0,0)}}$$

with $K = (2K_1 + 1)(2K_2 + 1) - 1$.

We consider two covariance matrix estimators on wavelet feature vectors: the standard sample covariance matrix (SCM) which can be written, under the zero-mean wavelet coefficient assumption, in the form

$$\hat{\mathbf{R}}_{\text{SCM},j}[p, q] = \frac{1}{K} \sum_{\substack{\ell_1=-K_1, \dots, K_1 \\ \ell_2=-K_2, \dots, K_2 \\ (\ell_1, \ell_2) \neq (0,0)}} \mathbf{c}_j[p - \ell_1, q - \ell_2] \times \mathbf{c}_j^H[p - \ell_1, q - \ell_2] \quad (20)$$

and, as an alternative to SCM (which can have poorer performance under generalized CES model assumption), the Tyler's estimator (TE), which has proven some robustness in both Gaussian and non-Gaussian cases and which is defined as the solution of the fixed-point equation [53] as shown in bottom of this page.

The TE estimator is robust to nonstationarities that are naturally present in HR SAR images.

For both SCM and TE estimators, the number K has to be around $K \approx 2N$ for a good estimation [41]. For high values of R or L , the vectors become very large. Sometimes, it would be impossible to have a sufficient number of secondary samples for the estimation of the covariance matrix. In those cases, regularized versions of SCM and TE exist in the literature and have shown good results for many applications [54]–[56].

Note that both estimators are used to estimate the covariance matrix of the clutter around a target. Hence, the test pixel (namely, $(\ell_1, \ell_2) \neq (0, 0)$) is excluded in the process.

B. Detection Schemes

We assume that a target with a known steering vector $\mathbf{p} \in \mathbb{C}^N$ could be present in some pixels in the SAR image.¹ We have for each pixel $I[p, q]$ to solve the standard binary hypothesis test

$$\begin{cases} H_0 : \mathbf{c}_j[p, q] = \mathbf{n}, & \mathbf{c}_k = \mathbf{n}_k \quad \forall k \in [1, K] \\ H_1 : \mathbf{c}_j[p, q] = a\mathbf{p} + \mathbf{n}, & \mathbf{c}_k = \mathbf{n}_k \quad \forall k \in [1, K] \end{cases} \quad (22)$$

where $(\mathbf{n}, \mathbf{n}_k)$ both represent a noise with the same distribution, a is an unknown complex amplitude of the potential target with spectroangular steering vector \mathbf{p} to be detected and $\{\mathbf{c}_k\}_{k \in [1, K]}$ being the K secondary data.

In this detection issue, we decide to test different adaptive detectors like the well-known adaptive matched filter which corresponds to a two-step generalized likelihood ratio test in homogeneous Gaussian noise [41]

$$\Lambda_j^{\text{AMF}}[p, q] = \frac{|\mathbf{p}^H \hat{\mathbf{R}}_{\text{SCM},j}^{-1}[p, q] \mathbf{c}_j[p, q]|^2}{\mathbf{p}^H \hat{\mathbf{R}}_{\text{SCM},j}^{-1}[p, q] \mathbf{p}} \underset{H_0}{\overset{H_1}{\gtrless}} \lambda \quad (23)$$

where λ is the detection threshold.

For partially homogeneous Gaussian noise or for CES distributed noises [52], the derivation of the detection problem leads to the ANMF [59], [60]

$$\begin{aligned} \Lambda_j^{\text{ANMF}}[p, q] &= \frac{|\mathbf{p}^H \hat{\mathbf{R}}_{\text{TE},j}^{-1}[p, q] \mathbf{c}_j[p, q]|^2}{(\mathbf{p}^H \hat{\mathbf{R}}_{\text{TE},j}^{-1}[p, q] \mathbf{p})(\mathbf{c}_j^H[p, q] \hat{\mathbf{R}}_{\text{TE},j}^{-1}[p, q] \mathbf{c}_j[p, q])} \underset{H_0}{\overset{H_1}{\gtrless}} \lambda. \end{aligned} \quad (24)$$

The AMF detector has the CFAR property relative to the Gaussian distribution, while the ANMF is CFAR for both Gaussian and CES distributions. This is an important property since it allows to select a detection threshold to ensure a probability of false alarm (P_{Fa}) independently of the data being tested.

Concerning the complexity of these methods, the limiting factor is the need to compute the inverse of the covariance matrix for both AMF and ANMF schemes. Then, if the number of coefficients is high, this operation becomes time-consuming [typically $O((R \times L)^3)$].

As for the implementation, the target detection schemes can be implemented using parallel computation: by splitting the image into several subimages and treating each one by a given thread, the computation time is greatly reduced. The simulations presented in Section V were done using a machine with two Intel Xeon CPU E5-2670 v3 at 2.30-GHz processors,

¹Note that when the steering vector is not known, it is possible to develop Bayesian target detection schemes using works such as [57], [58].

$$\hat{\mathbf{R}}_{\text{TE},j}[p, q] = \frac{N}{K} \sum_{\substack{\ell_1=-K_1, \dots, K_1 \\ \ell_2=-K_2, \dots, K_2 \\ (\ell_1, \ell_2) \neq (0,0)}} \frac{\mathbf{c}_j[p - \ell_1, q - \ell_2] \mathbf{c}_j^H[p - \ell_1, q - \ell_2]}{\mathbf{c}_j^H[p - \ell_1, q - \ell_2] \hat{\mathbf{R}}_{\text{TE},j}^{-1}[p, q] \mathbf{c}_j[p - \ell_1, q - \ell_2]}$$

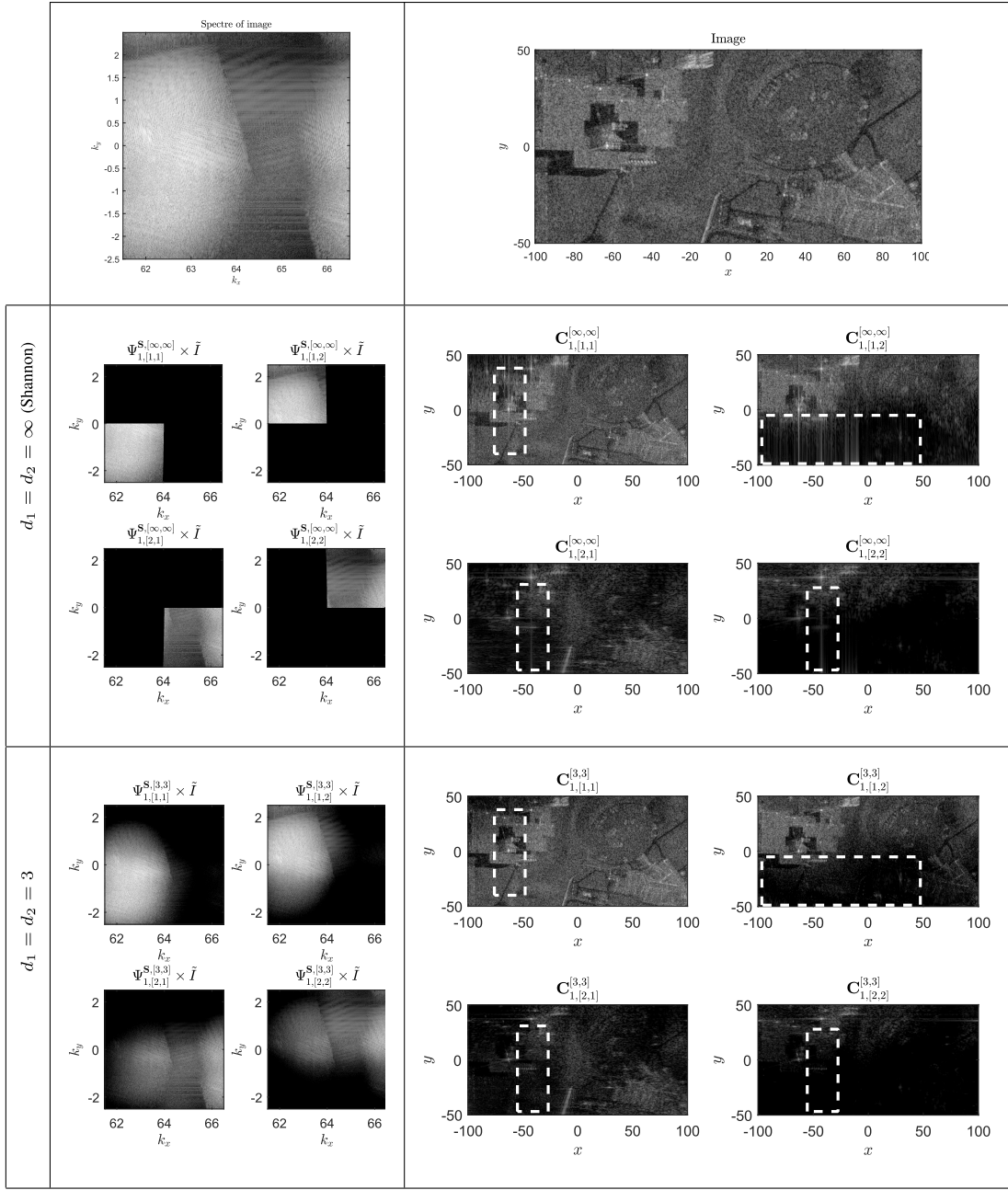


Fig. 8. Coefficients for Shannon and Bell-shaped wavelets on SDMS Image with $R = 2$ and $L = 2$. The improvement in terms of linear patterns (side lobes of bright points) for $d_1 = d_2 = 3$ are highlighted using dashed boxes.

that makes 24 cores in total, and 32 Gb of RAM, the computation time for an image of size 2510×1638 and $R = 5$, $L = 5$, was 3.35 s for the AMF algorithm and 28.34 s for the ANMF one.

V. SIMULATION AND RESULTS

Some simulation results and discussions on several aspects of wavelet analysis and target detection are presented here.

A. Data Set

Two data sets have been used to test the wavelet decompositions and their impact on target detection schemes.

- 1) SANDIA data set, available at http://www.sandia.gov/radar/complex_data/. The image referenced as *MiniSAR20050519p0010image002* is selected.
- 2) Sensor data management system (SDMS) data set [61], available at https://www.sdms.afrl.af.mil/index.php?collection=ccd_challenge. The image referenced as *FP0120* is selected.

Table I summarizes the information on both data sets.

B. Simulation Description

For a given SAR image, an artificial target with a given steering vector (representing its spectroangular behavior)

TABLE I
DESCRIPTION OF DATA SET

| Dataset | Band | Frequency | Resolution | Scene description |
|---------|------|-----------|------------|------------------------------|
| SANDIA | Ku | 16.8 GHz | 0.10 m | Stationary aircraft, trees |
| SDMS | X | 9.6GHz | 0.20 m | Foliage, buildings, vehicles |

is embedded. This allows controlling both position and signal-to-noise ratio (SNR) of the target to be detected. For a given image I , steering vector $\mathbf{p} \in \mathbb{C}^{R \times L}$, a pixel $[i_t, j_t]^T$ corresponding to position $\mathbf{r}_t = [\mathbf{x}(i_t), \mathbf{y}(j_t)]^T$ and a given SNR in decibels, an image with the target is obtained through

$$I_t = I + \frac{T}{\|T\|_{l_2}} \sigma 10^{\frac{\text{SNR}_{\text{dB}}}{20}} \quad (25)$$

with

$$T = \sum_{\substack{m=0, \dots, R^j-1 \\ n=0, \dots, L^j-1}} \mathcal{F}^{-1}\{p[m, n] \mathbb{I}_{\Delta_{j, R_m} \times \Delta_{j, \theta_n}} e^{i 2\pi \mathbf{k}^T \mathbf{r}_t}\}$$

and

$$\sigma^2 = \sum_{i=-10, \dots, 10} I(i_t + i, j_t + i)^2$$

the variance of the noise on a window around the target.

This process is done as follows.

- 1) Choose a steering vector \mathbf{p} .
- 2) Build spectrum according to the steering vector and create an image of the targets using (25).
- 3) Perform the wavelet decomposition and create the hyper-image using (13).
- 4) Apply the detectors (23), (24) with the given steering vector.

C. Results

1) *Spectroangular Behavior*: Fig. 8 shows a 2-Band 2-Look decomposition of a portion of SDMS Image. First, the spectroangular behavior of the data can be analyzed; given the subimage considered, different patterns emerge. Indeed, for example, the object in the bottom right corner of the figure ($0 > x > 100$ and $-50 < y < 0$), is not present in the coefficients $\mathbf{C}_{1,[1,2]}$ and $\mathbf{C}_{1,[2,2]}$.

2) *Quality of Decomposition*: Next, the wavelet decomposition is compared with two parameters d_1 and d_2 . When comparing both Shannon and Bell decomposition in Fig. 8, we observe for Shannon wavelets linear patterns (side lobes for the strong scatterers present in the scene). When considering $d_1 = d_2 = 3$, the undesired linear patterns are less prominent. This result was expected as Bell-shaped wavelets make a more concise decomposition in the spatial domain.

3) *P_{FA} - λ Curves*: Next, we plot in Fig. 9, the P_{FA} - λ (probability of false alarm versus threshold of detection) plots for both AMF and ANMF detectors to study the CFAR behavior of the detectors on the data sets. We choose a random steering vector and apply detectors on the image without any target. It can be observed that the ANMF detector fares a lot better in terms of regulation of false alarm than the AMF.

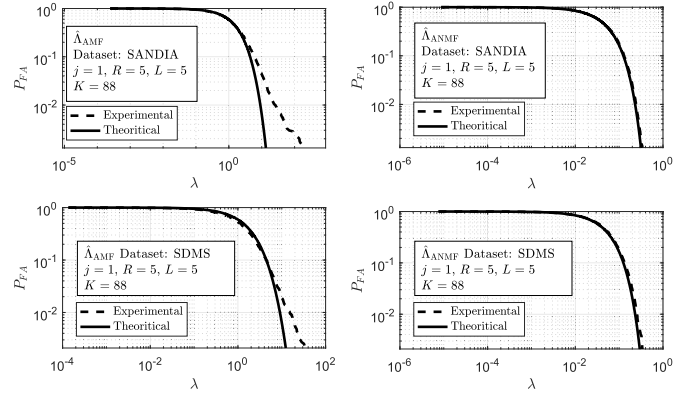


Fig. 9. P_{FA} - λ curves. $d_1 = d_2 = \infty$. (Left) AMF. (Right) ANMF. (Top) SANDIA data set, (Bottom) SDMS data set.

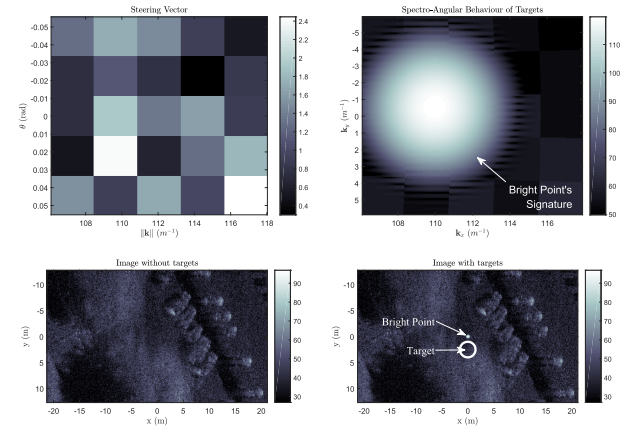


Fig. 10. Target near a bright point. Data set is SANDIA, $R = L = 5$. The target has an amplitude of -60 dB when compared to the bright point.

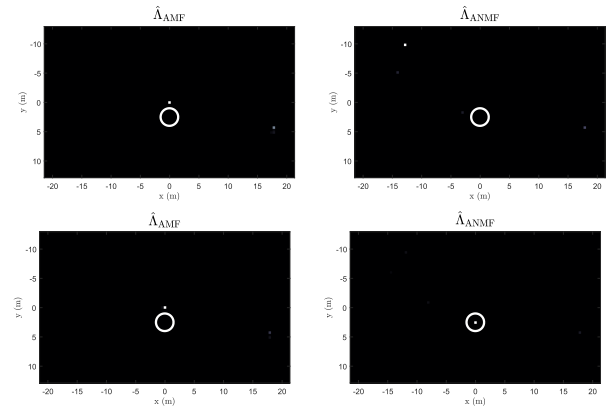


Fig. 11. Results at $P_{FA} = 10^{-3}$. (Top) $d_1 = d_2 = \infty$. (Bottom) $d_1 = d_2 = 10$. Data set is SANDIA, $R = L = 5$. The target has an amplitude of -60 dB when compared to the bright point.

When compared to the theoretical relationship, the AMF detector has an experimental threshold higher at low P_{FA} whereas the ANMF detector stays close to its theoretical performance. This can be interpreted by the heterogeneous nature of the data sets which is not well modeled by Gaussian assumption.

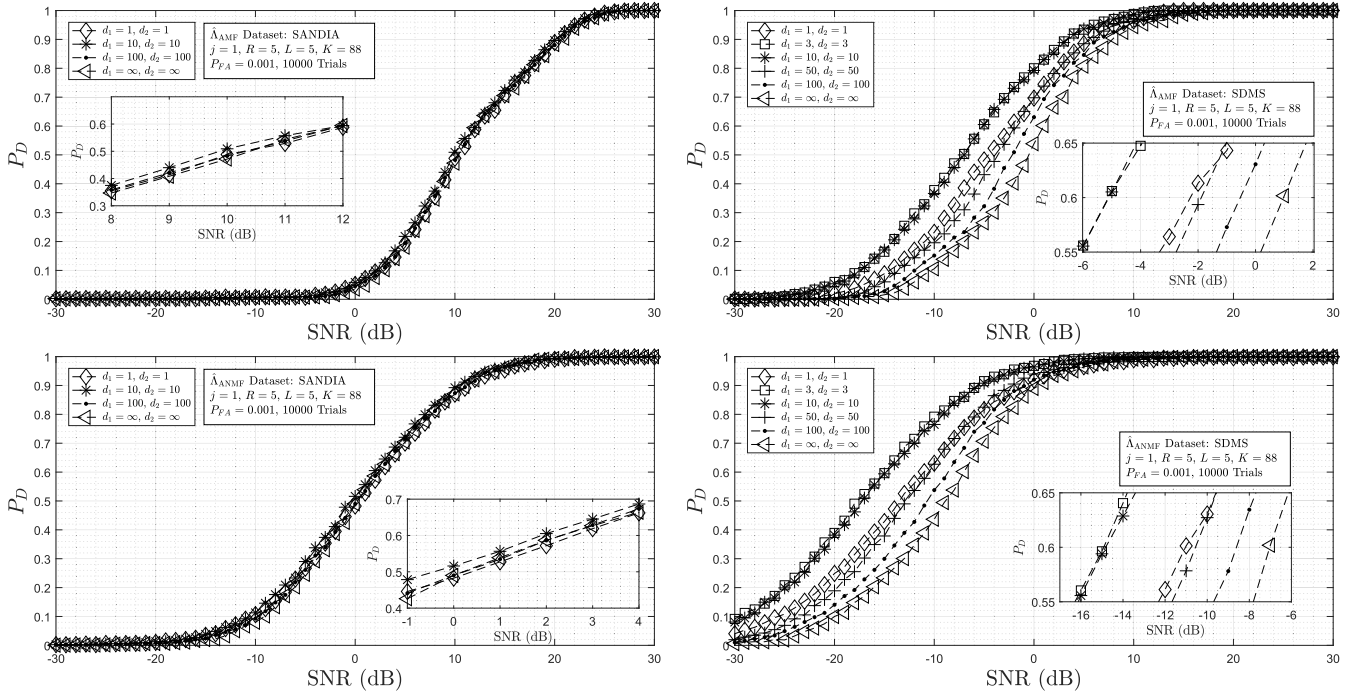


Fig. 12. P_d -SNR plots for several values of $d_1 = d_2$. (Top) AMF Detector. (Bottom) ANMF Detector.

TABLE II

RESULTS OF DETECTION WHEN RANDOMIZING STEERING VECTOR.
SNR = 0 dB, 100 DIFFERENT SIGNATURES HAVE BEEN TESTED
FOR 100 DIFFERENT TARGET POSITIONS ON EACH IMAGE

| SDMS | | | | | SANDIA | | | | |
|------|----------------|-------------|-------------|----------|----------------|-------------|-------------|-------------|--|
| | | mean | min | max | | mean | min | max | |
| AMF | $d_1 = 10$ | 0.81 | 0.67 | 0.91 | $d_1 = 10$ | 0.04 | 0 | 0.11 | |
| | $d_1 = \infty$ | 0.55 | 0.42 | 0.70 | $d_1 = \infty$ | 0.02 | 0 | 0.10 | |
| ANMF | $d_1 = 10$ | 0.95 | 0.89 | 1 | $d_1 = 10$ | 0.50 | 0.34 | 0.71 | |
| | $d_1 = \infty$ | 0.79 | 0.68 | 0.92 | $d_1 = \infty$ | 0.46 | 0.22 | 0.66 | |

4) *Detection Near Bright Point*: We choose $R = L = 5$ and $j = 1$ and we place the target to be detected, with an SNR of 20 dB, near a synthetic bright point with Gaussian spectro-angular behavior. Fig. 10 gives the steering vector of the target to detect, the specter of both targets and the image obtained by the procedure presented at V-B. The data set used here is the SANDIA one.

Then, we apply both detectors on the wavelet coefficients characterized by $d_1 = d_2 = \infty$ and $d_1 = d_2 = 10$. Fig. 11 shows the result of the detection at $P_{FA} = 10^{-3}$. The threshold guaranteeing the P_{FA} was taken from the experimental curves of Fig. 9.

Discussion: We focus first on the test of detection with $d_1 = d_2 = \infty$ (top of the figure). It can be observed that that for both detectors, the target is not detected. The AMF detector gives a false alarm at the position of the bright point, which is expected given that this detector is mostly a power-based detector. However, the ANMF detector does not detect the bright point as it does not have a similar spectroangular behavior as the steering vector. However, a false alarm is still present which can be explained by a similar of the

scene signature than the steering vector. If we take a look at detection tests for $d_1 = d_2 = 10$ (bottom of the figure), we observe that the target is detected with the ANMF detector but not the AMF one. This can be explained by the fact that with $d_1 = d_2 = 10$, we have reduced the side lobes of the bright point which does not pollute the pixel of the target any more resulting in better detection. The AMF detector does not yield better results for the same reason as previously.

These results are interesting since they confirm that the parameterization of the wavelet decomposition impacts the performance of detection.

5) *P_D -SNR Curves*: By randomizing the spatial location of the target for Monte Carlo trials, we obtain P_D -SNR plots for both detectors presented in Fig. 12. The steering vector is set to a fixed value for all the trials.

Discussion: We first observe that the ANMF detector performs better in terms of detection than the AMF one for both data sets: if we look at $P_D = 0.7$, a gain of almost 7 dB is observed for the ANMF for SDMS data set and 10 dB for SANDIA data set. This can be interpreted by the non-Gaussian nature of the data which makes regulation of false alarm difficult for the AMF detector and by the fact that ANMF is better suited for heterogeneous data.

The plots for the SANDIA data set show overall lower performance than the SDMS data set. This can be explained by the different nature of the data sets: the SANDIA image is more heterogeneous than the SDMS one and the speckle noise is more important.

Next, the different plots for each $d_1 = d_2$, lead to a significant gain when considering $d_1 = d_2 = 3$ or 10 compared to $d_1 = d_2 = \infty$ for the SDMS data set (about 8 dB at

$P_D = 0.6$). This result is coherent with the observations done previously in V-C4. Indeed, the side lobes are contained in the secondary data that is used for the estimation of the covariance matrix. These outliers lead to a loss of accuracy in the estimation which, in turn, decrease the performances of detection. It can be also observed a loss in detection for $d_1 = d_2 = 1$. This is coherent with the analysis of the previous section.

The gain using the new wavelet is lower on the SANDIA image (about 1 dB at $P_D = 0.6$). It is to be expected since the SANDIA data set contains few bright points spread over the scene.

6) *Impact of the Steering Vector*: In order to assess the impact of the steering vector, another Monte Carlo simulation has been done by setting the SNR to 0 dB and randomizing the target signature at each trial. For each trial, the target has been set to 100 different locations to compute a probability of detection. Table II gives the performance of detection for two values of $d_1 = d_2$ and for both data sets. The same conclusions as previously can be drawn: the ANMF detector performs better than the AMF one on both data sets and using a Bell-shaped wavelet with a parameter $d_1 = d_2 = 10$ allows improving the detection rate.

VI. CONCLUSION

This paper presented an adaptation of Shannon wavelet packets to SAR geometry in order to retrieve a physical diversity of interest. To reduce the side lobes, which are inherent to wavelet decomposition, a new family of parameterized wavelets has been proposed. These wavelets have the Shannon wavelets as a limit case and are tuned using a redundancy criterion.

This wavelet decomposition has been used in target detection schemes. It has been shown that the spectroangular diversity, inherent to HR SAR Images, can be used in classic adaptive detection framework. First, the robust framework has proven to be more effective over the Gaussian one in both false alarms regulation and performance of detection. Then, the reduction of side lobes with the new family of wavelets, yields significantly gain in the performance of detection when the image contains numerous bright points.

In this paper, we restrained ourselves to a fixed resolution-level for the statistical analysis. It may be interesting to use the multiresolution framework to selection a decomposition which yields the best possible diversity of a given image while keeping the size of vector low. To this end, a solution can be for example the use of an entropy-based criterion when doing the decomposition.

APPENDIX A PROOF OF PROPOSITION 1

Proof: Defining the wavelet coefficients from the following integral:

$$\mathbf{C}_{j,[n_1,n_2]}^S[p, q] = \iint_{\mathbb{R}^2} g(z, t) \tau_{[M_1^j p, M_2^j q]} \Phi_{j,[n_1,n_2]}^S(z, t) dz dt$$

we have (through Parseval)

$$\mathbf{C}_{j,[m,n]}^S[p, q] = \frac{1}{4\pi} \iint \mathcal{F}g(\omega_1, \omega_2) \overline{\mathcal{F}\tau_{[M_1^j p, M_2^j q]} \Phi_{j,[m,n]}^S}(\omega_1, \omega_2) d\omega_1 d\omega_2.$$

As (Fourier transform property on the translation)

$$\overline{\mathcal{F}\tau_{[M_1^j p, M_2^j q]} \Phi_{j,[m,n]}^S}(\omega_1, \omega_2) = e^{i(M_1^j p \omega_1)} e^{i(M_2^j q \omega_2)} \times \mathcal{F}\Phi_{j,[m,n]}^S(\omega_1, \omega_2)$$

we obtain

$$\mathbf{C}_{j,[m,n]}^S[p, q] = \frac{1}{4\pi} \iint e^{i(M_1^j p \omega_1)} e^{i(M_2^j q \omega_2)} \mathcal{F}g \mathcal{F}\Phi_{j,[m,n]}^S(\omega_1, \omega_2) d\omega_1 d\omega_2.$$

The integral corresponds to the 2-D inverse Fourier transform of $[\mathcal{F}g] \Psi_{j,[m,n]}^S$. ■

APPENDIX B PROOFS OF III-B

Proof of Proposition 2: Function $\Phi_{j,[m,n]}^{S,\angle}(x, y)$ being separable with respect to x and y , we have

$$\begin{aligned} \iint_{\mathbb{R}^2} x^p y^q \Phi_{j,[m,n]}^S(x, y) dx dy \\ = -i^{p+q} \frac{d}{d\mathfrak{R}} \frac{d}{d\theta} \Psi_{j,[m,n]}^{S,\angle}(\mathfrak{R}, \theta) \Big|_{\mathfrak{R}=0, \theta=0}. \end{aligned}$$

Proposition 2 follows by noting that $\Psi_{j,[m,n]}^S$ has null derivatives. ■

Proof of Proposition 3:

$$\begin{aligned} \langle \Phi_{j,[m,n]}^{S,\angle}, \Phi_{j,[m',n']}^{S,\angle} \rangle \\ = \iint_{\mathbb{R}^2} \Phi_{j,[m,n]}^{S,\angle}(x, y) \overline{\Phi_{j,[m',n']}^{S,\angle}(x, y)} dx dy. \end{aligned}$$

By using Parseval formula, we derive

$$\begin{aligned} \langle \Phi_{j,[m,n]}^{S,\angle}, \Phi_{j,[m',n']}^{S,\angle} \rangle \\ = \frac{1}{4\pi^2} \iint_{\mathbb{R}^2} \mathcal{F}\Phi_{j,[m,n]}^{S,\angle}(\mathfrak{R}, \theta) \overline{\mathcal{F}\Phi_{j,[m',n']}^{S,\angle}(\mathfrak{R}, \theta)} d\mathfrak{R} d\theta \end{aligned}$$

which reduces to

$$\begin{aligned} \langle \Phi_{j,[m,n]}^{S,\angle}, \Phi_{j,[m',n']}^{S,\angle} \rangle \\ = \frac{R^j L^j}{4\pi^2} \iint_{\mathbb{R}^2} \mathbb{I}_{\Delta_{j,\mathfrak{R}_m} \times \Delta_{j,\theta_n}}(\mathfrak{R}, \theta) \mathbb{I}_{\Delta_{j,\mathfrak{R}_{m'}} \times \Delta_{j,\theta_{n'}}}(\mathfrak{R}, \theta) d\mathfrak{R} d\theta. \end{aligned}$$

For $m \neq m'$ or $n \neq n'$, intersection $\Delta_{j,\mathfrak{R}_m} \times \Delta_{j,\theta_n} \cap \Delta_{j,\mathfrak{R}_{m'}} \times \Delta_{j,\theta_{n'}}$ of the supports of $\mathcal{F}\Phi_{j,[m,n]}^S$ and $\mathcal{F}\Phi_{j,[m',n']}^S(\mathfrak{R}, \theta)$ are either disjoint, or reduce to a null set. This ends the proof. ■

Proof of Proposition 4: The proof is a consequence of Shannon band-limited function representation and the fact that for any $j \geq 1$, the sets $\Delta_{j,\mathfrak{R}_m} \times \Delta_{j,\theta_n}$, for $m = 0, 1, \dots, R^j - 1$ and $n = 0, 1, \dots, L^j - 1$, are constructed so as to form a partition of \mathcal{D} . ■

APPENDIX C PROOFS OF III-C

Proof of Proposition 7: It suffices to show that $\lim_{d_1, d_2 \rightarrow +\infty} \Psi_{0, [0,0]}^{[d_1, d_2], \angle} = \Psi_{0, [0,0]}^{S, \angle}$. From (17), we have

$$H_{0, [0,0]}^{[d_1, d_2]}(\mathfrak{K}, \theta) = \frac{1}{1 + \left| \frac{2}{\mathfrak{K}_B} (\mathfrak{K} - \mathfrak{K}_0) \right|^{2d_1}} \frac{1}{1 + \left| \frac{\theta}{\theta_B} \right|^{2d_2}} \quad (26)$$

As a consequence, if $|\mathfrak{K} - \mathfrak{K}_0| < (\mathfrak{K}_B/2)$ and $|\theta| < \theta_B$, then

$$\lim_{d_1, d_2 \rightarrow +\infty} H_{0, [0,0]}^{[d_1, d_2]}(\mathfrak{K}, \theta) = 1.$$

In contrast, if $|\mathfrak{K} - \mathfrak{K}_0| > (\mathfrak{K}_B/2)$ or $|\theta| > \theta_B$, then

$$\lim_{d_1, d_2 \rightarrow +\infty} H_{0, [0,0]}^{[d_1, d_2]}(\mathfrak{K}, \theta) = 0$$

which ends the proof. ■

REFERENCES

- [1] W. G. Carrara, R. S. Goodman, and R. M. Majewski, *Spotlight Synthetic Aperture Radar: Signal Processing Algorithms*. Norwood, MA, USA: Artech House, 1995.
- [2] J. Bertrand and P. Bertrand, "The concept of hyperimage in wide-band radar imaging," *IEEE Trans. Geosci. Remote Sens.*, vol. 34, no. 5, pp. 1144–1150, Sep. 1996.
- [3] M. Duquenoy, J. P. Ovarlez, L. Ferro-Famil, L. Vignaud, and E. Pottier, "Study of dispersive and anisotropic scatterers behavior in radar imaging using time-frequency analysis and polarimetric coherent decomposition," in *Proc. IEEE Radar Conf.*, Verona, NY, USA, Apr. 2006, pp. 180–185.
- [4] J. Li and E. G. Zelnio, "Target detection with synthetic aperture radar," *IEEE Trans. Aerosp. Electron. Syst.*, vol. 32, no. 2, pp. 613–627, Apr. 1996.
- [5] Z. Tirandaz and G. Akbarizadeh, "A two-phase algorithm based on kurtosis curvelet energy and unsupervised spectral regression for segmentation of SAR images," *IEEE J. Sel. Topics Appl. Earth Observ. Remote Sens.*, vol. 9, no. 3, pp. 1244–1264, Mar. 2016.
- [6] M. Rahmani and G. Akbarizadeh, "Unsupervised feature learning based on sparse coding and spectral clustering for segmentation of synthetic aperture radar images," *IET Comput. Vis.*, vol. 9, no. 5, pp. 629–638, 2015.
- [7] G. Akbarizadeh, "A new statistical-based kurtosis wavelet energy feature for texture recognition of SAR images," *IEEE Trans. Geosci. Remote Sens.*, vol. 50, no. 11, pp. 4358–4368, Nov. 2012.
- [8] D. Karimi, G. Akbarizadeh, K. Rangzan, and M. Kabolizadeh, "Effective supervised multiple-feature learning for fused radar and optical data classification," *IET Radar, Sonar Navigat.*, vol. 11, no. 5, pp. 768–777, 2017.
- [9] G. Akbarizadeh, "A new recognition approach based on genetic algorithm for classifying textures in satellite SAR images," *Int. J. Remote Sens. Appl.*, vol. 2, no. 4, pp. 7–19, 2012.
- [10] D. Karimi, K. Rangzan, G. Akbarizadeh, and M. Kabolizadeh, "Combined algorithm for improvement of fused radar and optical data classification accuracy," *J. Electron. Imag.*, vol. 26, no. 1, p. 013017, 2017.
- [11] H. Rohling, "Radar CFAR thresholding in clutter and multiple target situations," *IEEE Trans. Aerosp. Electron. Syst.*, vol. AES-19, no. 4, pp. 608–621, Jul. 1983.
- [12] A. Sharma and R. L. Moses, "Matched subspace detectors for discrimination of targets from trees in SAR imagery," in *Proc. Conf. Rec. 34th Asilomar Conf. Signals, Syst. Comput.*, vol. 2, Oct. 2000, pp. 1721–1726.
- [13] A. Izzo, M. Liguori, C. Clemente, C. Galdi, M. D. Bisceglie, and J. J. Soraghan, "Multimodel CFAR detection in foliage penetrating SAR images," *IEEE Trans. Aerosp. Electron. Syst.*, vol. 53, no. 4, pp. 1769–1780, Aug. 2017.
- [14] D. Pastina, P. Lombardo, A. Farina, and P. Daddi, "Super-resolution of polarimetric SAR images of ship targets," *Signal Process.*, vol. 83, no. 8, pp. 1737–1748, 2003.
- [15] A. Alonso-González, C. López-Martínez, and P. Salembier, "Filtering and segmentation of polarimetric SAR data based on binary partition trees," *IEEE Trans. Geosci. Remote Sens.*, vol. 50, no. 2, pp. 593–605, Feb. 2012.
- [16] D. Ratha, A. Bhattacharya, and A. C. Frery, "Unsupervised classification of PolSAR data using a scattering similarity measure derived from a geodesic distance," *IEEE Geosci. Remote Sens. Lett.*, vol. 15, no. 1, pp. 151–155, Jan. 2018.
- [17] F. Bandiera, M. Jahangir, G. Ricci, and R. Verrienti, "Adaptive radar detection without secondary data: Exploiting a diversity idea," in *Proc. 14th Eur. Signal Process. Conf.*, Sep. 2006, pp. 1–5.
- [18] D. Cerutti-Maori, I. Sikaneta, and C. H. Gierull, "Optimum SAR/GMTI processing and its application to the radar satellite RADARSAT-2 for traffic monitoring," *IEEE Trans. Geosci. Remote Sens.*, vol. 50, no. 10, pp. 3868–3881, Oct. 2012.
- [19] S.-X. Zhang, M.-D. Xing, X.-G. Xia, R. Guo, Y.-Y. Liu, and Z. Bao, "Robust clutter suppression and moving target imaging approach for multichannel in azimuth high-resolution and wide-swath synthetic aperture radar," *IEEE Trans. Geosci. Remote Sens.*, vol. 53, no. 2, pp. 687–709, Feb. 2015.
- [20] D. Li, M. Zhan, J. Su, H. Liu, X. Zhang, and G. Liao, "Performances analysis of coherently integrated CPF for LFM signal under low SNR and its application to ground moving target imaging," *IEEE Trans. Geosci. Remote Sens.*, vol. 55, no. 11, pp. 6402–6419, Nov. 2017.
- [21] B. Liu, K. Yin, Y. Li, F. Shen, and Z. Bao, "An improvement in multichannel SAR-GMTI detection in heterogeneous environments," *IEEE Trans. Geosci. Remote Sens.*, vol. 53, no. 2, pp. 810–827, Feb. 2015.
- [22] I. C. Sikaneta and C. H. Gierull, "Adaptive CFAR for space-based multichannel SAR-GMTI," *IEEE Trans. Geosci. Remote Sens.*, vol. 50, no. 12, pp. 5004–5013, Dec. 2012.
- [23] A. Taylor, P. Forster, F. Daout, H. M. Oriot, and L. Savy, "A generalization of the fixed point estimate for packet-scaled complex covariance matrix estimation," *IEEE Trans. Signal Process.*, vol. 65, no. 20, pp. 5393–5405, Oct. 2017.
- [24] E. P. Simoncelli, W. T. Freeman, E. H. Adelson, and D. J. Heeger, "Shiftable multiscale transforms," *IEEE Trans. Inf. Theory*, vol. 38, no. 2, pp. 587–607, Mar. 1992.
- [25] M. Unser, N. Chenouard, and D. Van De Ville, "Steerable pyramids and tight wavelet frames in $L_2(\mathbb{R}^d)$," *IEEE Trans. Image Process.*, vol. 20, no. 10, pp. 2705–2721, Oct. 2011.
- [26] E. Candès, L. Demanet, D. Donoho, and X. Ying, "Fast discrete curvelet transforms," *Multiscale Model. Simul.*, vol. 5, no. 3, pp. 861–899, Sep. 2006.
- [27] R. Durand, G. Ginolhac, L. Thirion, and P. Forster, "New SAR processor based on matched subspace detectors," *IEEE Trans. Aerosp. Electron. Syst.*, vol. 45, no. 1, pp. 221–236, Jan. 2009.
- [28] F. Brigui, L. Thirion-Lefevre, G. Ginolhac, and P. Forster, "New SAR algorithm based on orthogonal projections for MMT detection and interference reduction," *IEEE Trans. Geosci. Remote Sens.*, vol. 52, no. 7, pp. 3800–3811, Jul. 2014.
- [29] C. Brekke, S. N. Anfinssen, and Y. Larsen, "Subband extraction strategies in ship detection with the subaperture cross-correlation magnitude," *IEEE Geosci. Remote Sens. Lett.*, vol. 10, no. 4, pp. 786–790, Jul. 2013.
- [30] G. D. D. Grandi, J. S. Lee, and D. L. Schuler, "Target detection and texture segmentation in polarimetric SAR images using a wavelet frame: Theoretical aspects," *IEEE Trans. Geosci. Remote Sens.*, vol. 45, no. 11, pp. 3437–3453, Nov. 2007.
- [31] G. D. D. Grandi, R. M. Lucas, and J. Kropacek, "Analysis by wavelet frames of spatial statistics in SAR data for characterizing structural properties of forests," *IEEE Trans. Geosci. Remote Sens.*, vol. 47, no. 2, pp. 494–507, Feb. 2009.
- [32] S. Zecchetto and F. D. Biasio, "A wavelet-based technique for sea wind extraction from SAR images," *IEEE Trans. Geosci. Remote Sens.*, vol. 46, no. 10, pp. 2983–2989, Oct. 2008.
- [33] C. Lopez-Martinez and X. Fabregas, "Modeling and reduction of SAR interferometric phase noise in the wavelet domain," *IEEE Trans. Geosci. Remote Sens.*, vol. 40, no. 12, pp. 2553–2566, Dec. 2002.
- [34] J. Ma, M. Gong, and Z. Zhou, "Wavelet fusion on ratio images for change detection in SAR images," *IEEE Geosci. Remote Sens. Lett.*, vol. 9, no. 6, pp. 1122–1126, Nov. 2012.
- [35] N. Subotic, L. Collins, J. D. Gorman, and B. Thelen, "A multiresolution approach to target detection in synthetic aperture radar data," in *Proc. 28th Asilomar Conf. Signals, Syst. Comput.*, vol. 1, Oct. 1994, pp. 122–126.
- [36] W. W. Irving, L. M. Novak, and A. S. Willsky, "A multiresolution approach to discrimination in SAR imagery," *IEEE Trans. Aerosp. Electron. Syst.*, vol. 33, no. 4, pp. 1157–1169, Oct. 1997.

- [37] M. Tria, J. P. Ovarlez, L. Vignaud, J. C. Castelli, and M. Benidir, "Discriminating real objects in radar imaging by exploiting the squared modulus of the continuous wavelet transform," *IET Radar, Sonar Navigat.*, vol. 1, no. 1, pp. 27–37, Feb. 2007.
- [38] J.-P. Ovarlez, L. Vignaud, J.-C. Castelli, M. Tria, and M. Benidir, "Analysis of SAR images by multidimensional wavelet transform," *IEE Proc.-Radar, Sonar Navigat.*, vol. 150, no. 4, pp. 234–241, Aug. 2003.
- [39] J.-P. Ovarlez, G. Ginolhac, and A. M. Atto, "Multivariate linear time-frequency modeling and adaptive robust target detection in highly textured monovariate SAR image," in *Proc. IEEE Int. Conf. Acoust., Speech Signal Process. (ICASSP)*, Mar. 2017, pp. 4029–4033.
- [40] A. Mian, J. P. Ovarlez, G. Ginolhac, and A. M. Atto, "Multivariate change detection on high resolution monovariate SAR image using linear time-frequency analysis," in *Proc. 25th Eur. Signal Process. Conf. (EUSIPCO)*, Kos, Greece, Aug./Sep. 2017, pp. 1942–1946.
- [41] F. C. Robey, D. R. Fuhrmann, E. J. Kelly, and R. Nitzberg, "A CFAR adaptive matched filter detector," *IEEE Trans. Aerosp. Electron. Syst.*, vol. 28, no. 1, pp. 208–216, Jan. 1992.
- [42] S. Kraut and L. L. Scharf, "The CFAR adaptive subspace detector is a scale-invariant GLRT," *IEEE Trans. Signal Process.*, vol. 47, no. 9, pp. 2538–2541, Sep. 1999.
- [43] E. Conte, M. Lops, and G. Ricci, "Adaptive detection schemes in compound-Gaussian clutter," *IEEE Trans. Aerosp. Electron. Syst.*, vol. 34, no. 4, pp. 1058–1069, Oct. 1998.
- [44] L. Denis, A. Ferrari, D. Mary, L. Mugnier, and E. Thiébaud, "Fast and robust detection of a known pattern in an image," in *Proc. 24th Eur. Signal Process. Conf. (EUSIPCO)*, Aug. 2016, pp. 2206–2210.
- [45] M. Duquenoy, J. P. Ovarlez, L. Ferro-Famil, E. Pottier, and L. Vignaud, "Scatterers characterisation in radar imaging using joint time-frequency analysis and polarimetric coherent decompositions," *IET Radar, Sonar Navigat.*, vol. 4, no. 3, pp. 384–402, Jun. 2010.
- [46] N. Hess-Nielsen, "Control of frequency spreading of wavelet packets," *Appl. Comput. Harmon. Anal.*, vol. 1, no. 2, pp. 157–168, Mar. 1994.
- [47] M. Nielsen, "Highly nonstationary wavelet packets," *Appl. Comput. Harmon. Anal.*, vol. 12, no. 2, pp. 209–229, Mar. 2002.
- [48] A. Averbuch, R. R. Coifman, D. L. Donoho, M. Elad, and M. Israeli, "Fast and accurate polar Fourier transform," *Appl. Comput. Harmon. Anal.*, vol. 21, no. 2, pp. 145–167, 2006.
- [49] O. Christensen, *An Introduction to Frames and Riesz Bases* (Applied and Numerical Harmonic Analysis). Basel, Switzerland: Birkhäuser, 2002.
- [50] A. Cohen, I. Daubechies, and J.-C. Feauveau, "Biorthogonal bases of compactly supported wavelets," *Commun. Pure Appl. Math.*, vol. 45, no. 5, pp. 485–560, 1992.
- [51] J. Kovacevic, P. L. Dragotti, and V. K. Goyal, "Filter bank frame expansions with erasures," *IEEE Trans. Inf. Theory*, vol. 48, no. 6, pp. 1439–1450, Jun. 2002.
- [52] E. Ollila, D. E. Tyler, V. Koivunen, and H. V. Poor, "Complex elliptically symmetric distributions: Survey, new results and applications," *IEEE Trans. Signal Process.*, vol. 60, no. 11, pp. 5597–5625, Nov. 2012.
- [53] F. Pascal, Y. Chitour, J.-P. Ovarlez, P. Forster, and P. Larzabal, "Covariance structure maximum-likelihood estimates in compound Gaussian noise: Existence and algorithm analysis," *IEEE Trans. Signal Process.*, vol. 56, no. 1, pp. 34–38, Jan. 2008.
- [54] Y. Chen, A. Wiesel, and A. O. Hero, "Robust shrinkage estimation of high-dimensional covariance matrices," *IEEE Trans. Signal Process.*, vol. 59, no. 9, pp. 4097–4107, Sep. 2011.
- [55] F. Pascal, Y. Chitour, and Y. Quek, "Generalized robust shrinkage estimator and its application to STAP detection problem," *IEEE Trans. Signal Process.*, vol. 62, no. 21, pp. 5640–5651, Nov. 2014.
- [56] E. Ollila and D. E. Tyler, "Regularized M -estimators of scatter matrix," *IEEE Trans. Signal Process.*, vol. 62, no. 22, pp. 6059–6070, Nov. 2014.
- [57] O. Besson, A. Coluccia, E. Chaumette, G. Ricci, and F. Vincent, "Generalized likelihood ratio test for detection of Gaussian rank-one signals in Gaussian noise with unknown statistics," *IEEE Trans. Signal Process.*, vol. 65, no. 4, pp. 1082–1092, Feb. 2017.
- [58] A. Coluccia and G. Ricci, "Adaptive radar detectors for point-like Gaussian targets in Gaussian noise," *IEEE Trans. Aerosp. Electron. Syst.*, vol. 53, no. 3, pp. 1284–1294, Jun. 2017.
- [59] S. Kraut, L. L. Scharf, and L. M. Whorther, "Adaptive subspace detector," *IEEE Trans. Signal Process.*, vol. 49, no. 1, pp. 1–16, Jan. 2001.
- [60] M. S. Greco and A. De Maio, Eds., *Modern Radar Detection Theory*. Rijeka, Croatia: SciTech, 2016.
- [61] S. M. Scarborough *et al.*, "A challenge problem for SAR change detection and data compression," *Proc. SPIE*, vol. 7699, p. 76990U, Apr. 2010.



Ammar Mian (S'18) received the master's degree in signal processing from the Grenoble INP, Grenoble, France, in 2016. He is currently pursuing the Ph.D. degree in signal processing with the CentraleSupélec, Gif-sur-Yvette, France.

His research interests include statistical signal processing, with a focus on the processing of remotely sensed images, time-frequency analysis, and machine learning.



Jean-Philippe Ovarlez (M'06) was born in Denain, France in 1963. He received jointly the engineering degree from Ecole Supérieure d'Electronique Automatique et Informatique (ESIEA), Paris, France and the Diplôme d'Etudes Approfondies degree in Signal Processing from University of Paris XI, Orsay, France and the Ph.D. degree in Physics from the University of Paris VI, Paris, France, in 1987 and 1992, respectively. In 2011, he obtained a Research Directorship Habilitation (HDR) thesis in Signal Processing from the University of Paris-Sud and his qualification to the University Professor position. In 1992, he joined the Electromagnetic and Radar Division of the French Aerospace Lab (ONERA), Palaiseau, France, where he is currently Chief Scientist and member of the Scientific Committee of the ONERA Physics Branch. Since 2008, he is attached at a part time to Centrale-Supélec SONDRALab, in charge of Signal Processing activities supervision. In 2015, he becomes member of Special Area Team (SAT) in Theoretical and Methodological Trends in Signal Processing (TMTSP), EURASIP and treasurer of the IEEE GRSS French Chapter in 2016. His research interests are centered in the topic of Statistical Signal Processing for radar and SAR applications such as Time-Frequency, imaging, detection and parameters estimation.



Abdourrahmane Mahamane Atto (M'09–SM'16) received the master's degree in applied mathematics and pure mathematics from the University of Abomey-Calavi, Abomey Calavi, Benin, in 2001 and 2002, respectively; the master's degree in advanced studies in electrical engineering from école Polytechnique d'Abomey-Calavi, Abomey Calavi, in 2002; the master's degree in image and artificial intelligence from TELECOM Bretagne, Brest, France, in 2005; the Ph.D. degree in applied mathematics from the University of Rennes I, Rennes, France, and TELECOM Bretagne, Rennes, in 2008; and the Habilitation degree for research supervision from Université Grenoble Alpes, Grenoble, France, in 2015.

From 2002 to 2003, he was with école Polytechnique d'Abomey-Calavi. From 2003 to 2004, he was with école des Mines, de l'Industrie et de la Géologie, Niamey, Niger. From 2008 to 2009, he was with TELECOM Bretagne. From 2009 to 2011, he was with the Institut Polytechnique de Bordeaux, Talence, France. Since 2011, he has been an Associate Professor with the Polytech Annecy-Chambéry, Université Savoie Mont Blanc, Annecy-Le-Vieux, France. His research interests include mathematical methods and models for signal, image, and information processing.



Guillaume Ginolhac (S'98–M'01–SM'12) received the master's degree in electrical engineer and the Ph.D. degree in signal processing from Grenoble-INP, Grenoble, France, in 1997 and 2001, respectively. His Research Directorship Habilitation (HDR) thesis was focused on signal processing from the ENS Cachan Institute, Cachan, France, in 2011.

From 2002 to 2012, he was an Associate Professor with the SATIE Lab, University Paris Nanterre, Nanterre, France. Since 2012, he has been a Full Professor with the LISTIC Lab, University Savoie Mont-Blanc, Chambéry, France. Since 2018, he has also been the Head of the Connaissances, Images, Télédétection Group, LISTIC Lab. His research interests include estimation and detection theory for statistical signal processing and applications to array processing and radar/sonar.